Supplementary Information for

Mesophase-induced Vitrification in Coordination Polymers via Aliphatic Chain Dynamics

Minhyuk Kim[1,3] Hoe-yeon Jeong[2], Yelim Lee[3], Eun-chae Jeon[2,], and Hoi Ri Moon[3,*]*

[1] Department of Chemistry, Ulsan National Institute of Science and Technology (UNIST), Ulsan 44919, Republic of Korea.

[2] School of Materials Science and Engineering, University of Ulsan, 93 Daehak-ro, Nam-gu, Ulsan 44610, Republic of Korea

[3] Department of Chemistry and Nanoscience, Ewha Womans University, Seoul 03760, Republic of Korea

*E-mail: jeonec@ulsan.ac.kr; hoirimoon@ewha.ac.kr

Supplementary Notes 1. Synthesis of *C*-MgC$_n$DCs and *desG*-MgC$_n$DCs

All reactants were purchased from Sigma-Aldrich and used without additional purification. ***C***-MgC$_n$DC series was synthesized using analogous procedures.

For each synthesis, 30.0 mmol of an aliphatic α, ω-dicarboxylic acid, (HOOC)(CH$_2$)$_n$(COOH) (n = 2–7), was dissolved or dispersed in 500 mL of deionized water with 500 rpm stirring. Then, 28.0 mmol of either Mg powder (680.5 mg) or Mg(OH)$_2$ (1632.9 mg) was added to the ligand solution. The mixture was stirred at room temperature (RT) for 10-20 min until the solution became completely transparent and then filtered. The filtrate was concentrated to yield a precipitate containing coordination polymers and unreacted ligands. The crude product was washed several times with acetone to remove residual ligands, affording pure ***C***-MgC$_n$DC. The ***C***-MgC$_n$DC samples were subsequently dried overnight in a vacuum oven at RT. The ***desG***-MgC$_n$DC samples were prepared by heating the dried ***C***-MgC$_n$DC powders to a temperature 5–10 °C above their respective T_g for 10 minutes, followed by quenching to room temperature.

Supplementary Notes 2. Thermal analyses of *C*-MgC$_n$DCs

All thermal analyses were performed under an Ar gas condition, preventing oxidation during the heating process. The samples were prepared in a dried powder form.

Thermogravimetric analysis (TGA) was performed at a ramp rate of 10 °C·min^{-1} to determine the dehydration temperatures and T_d, using a TGA Q50 from TA Instruments.

Differential scanning calorimetry (DSC) experiments were performed using a DSC25 from TA Instruments.

Temperature-modulated DSC (TMDSC) were performed by MDSC® using a DSC25 from TA instruments. All measurements applied modulated heat-only mode at an average ramp rate of 2 °C·min^{-1} and modulated temperature 0.637 °C for 120 seconds. The T_g and T_c of MgC$_n$DC series were defined as the onset temperature of the glass transition peak in reversing heat flow graph and the cold crystallisation peak in non-reversing heat flow graph. The T_{lc} and T_m of MgC$_7$DC were identified from the endothermic ***desL***-to-***LC*** transition peak and the melting peak.

Supplementary Notes 3. Characterization of MgC_nDCs

X-ray powder diffraction (XRPD) data were collected on a Bruker D2 phaser diffractometer at 30 kV and 10 mA for Cu K_α (λ = 1.54050 Å), with a step size of 0.02° in 2θ.

Time-resolved in-situ XRPD measurements were performed on the BL13XU beamline at the Super photon ring-8 GeV (SPring-8, Hyogo, Japan) for 59.0 keV (λ = 0.21014 Å), with a step size of 0.005° in 2θ (scan range, 0.600–76.545°). The samples were prepared under a N_2 atmosphere and then loaded in borosilicate glass capillaries with a diameter of 1 mm and sealed with flame.

Solution ^1H Fourier-transform NMR experiments were carried out on an AVANCE III 300 from Bruker, at the Basic Sciences Research Institute (BSRI) in Ewha Womans University. All samples were prepared after digestion using deuterium chloride solution (35%, in D_2O) and then dissolved in DMSO-d_6 solvent.

Infrared spectra were recorded with a ThermoFisher Scientific iS10 FT-IR spectrometer using attenuated total reflectance mode.

X-ray total scattering data were collected on the BL04B2 and BL13XU beamline at SPring-8. The samples were prepared under a N_2 atmosphere and then loaded in borosilicate or Lindeman glass capillaries with a diameter of 1 mm and sealed with flame. The incident wavelength X-ray for BL04B2 was 112.4 keV (λ = 0.11030 Å), with a step size of 0.02° in 2θ (scan range, 0.200–29.100°), and for BL13XU for 59.0 keV as described above. The collected data were corrected for polarization, absorption, background, and Compton scattering, and then used to obtain the Faber-Ziman total structure factor $S(Q)$.

From each $S(Q)$, pair distribution functions (PDF) in the form $G(r)$ were calculated using a Lorch function in the BL04B2anaGUI with Igor Pro software. The maximum range of data (Q_{max}) used in the Fourier transform to obtain $G(r)$ was 22 $Å^{-1}$. PDF data provided information on short- and long-range order correlations (up to at r ~ 100 Å) for all samples.

Supplementary Tables

Supplementary Table 1. Abbreviations, descriptions, and thermal conditions for the different states of the MgC$_n$DC series.

Abbreviations	States	Temperature region	Samples (n)
C-	Pristine crystal	-	All (n = 2–7)
desC-	Desolvated crystal (Crystalline mesophase)	$T_{des} < T < T_g$	All (n = 2–7)
desL-	Supercooled liquid state of ***desC***-MgC$_n$DCs	$T > T_g$	n = 3–7
desG-	Quenched glass from ***desL***-MgC$_n$DCs (*Mesophase glass*)	Quenched from $T > T_g$	n = 3–7
reC-	Cold-crystallised phase from ***desL***-MgC$_n$DCs	$T > T_c$	n = 2–5
LC-	Liquid crystal phase from ***desL***-MgC$_7$DC	$T > T_{lc}$	Only n = 7
mqG-	Melt-quenched glass from molten MgC$_7$DC	Quenched from $T > T_m$	Only n = 7

Supplementary Table 2. Summary of molecular formulas, weights, and TGA results for the MgC_nDC series.

	Molecular formula of the ***C***- state	M.W. of ***C***- state	M.W. without H_2O	Theoretical residual wt%[a]	Measured wt%[b]
C-MgC_2DC	$[Mg(CH_2)_2(COO)_2(H_2O)_4]$	212.4	140.3	66.05%	63.71%
C-MgC_3DC	$[Mg(CH_2)_3(COO)_2(H_2O)_4]$	226.4	154.4	68.19%	68.15%
C-MgC_4DC	$[Mg(CH_2)_4(COO)_2(H_2O)_4]$	240.4	168.4	70.05%	69.81%
C-MgC_5DC	$[Mg(CH_2)_5(COO)_2(H_2O)_3]$	236.5	182.4	77.12%	82.72%[c]
C-MgC_6DC	$[Mg(CH_2)_6(COO)_2(H_2O)_3]$	250.5	196.4	78.40%	78.15%
C-MgC_7DC	$[Mg(CH_2)_7(COO)_2(H_2O)_3]$	264.5	210.5	79.58%	79.55%

[a] Calculated as: (M.W. without H_2O / M.W. of ***C***- state)*100%.

[b] From TGA results of MgC_nDCs at 250 °C.

[c] The measured weight (82.72%) is more consistent with the formation of a monohydrate state, $[Mg(C_5DC)(H_2O)]$ (M. W. = 200.6, wt% = 84.82%).

Supplementary Table 3. Characteristic FTIR wavenumbers for the $\nu_{as}(CH_2)$ and $\nu_{as}(COO)$ modes of MgC_nDCs in various phases.

$\nu_{as}(CH_2)$ / cm^{-1}	***C-***	***desC-***	***desG-***	***reC-***	***Δ(desC-C)***	***Δ(desG-desC)***	***Δ(reC-desG)***
MgC_2DC	-[a]	2979.73	-[a]	2969.33	-	-	-
MgC_3DC	2977.24	-[a]	2942.50	2941.58	-	-	-0.92
MgC_4DC	2956.07	2936.71	2934.69	2929.72	-19.36	-2.02	-4.97
MgC_5DC	2928.50	2932.55	2932.13	2927.34	4.05	-0.42	-4.79
MgC_6DC	2939.13	2928.58	2929.74	-	-10.55	1.16	-
MgC_7DC	2919.80	2927.43	2925.65	-	7.63	-1.78	-

$\nu_{as}(COO)$ / cm^{-1}	***C-***	***desC-***	***desG-***	***reC-***	***Δ(desC-C)***	***Δ(desG-desC)***	***Δ(reC-desG)***
MgC_2DC	1530.77	1574.40	-[a]	1605.61	43.63	-	-
MgC_3DC	1557.26	-[a]	1574.06	1600.50	-	-	26.44
MgC_4DC	1519.97	1574.37	1574.10	1592.21	54.40	-0.27	18.11
MgC_5DC	1556.92	1580.2	1582.77	1583.77	23.28	-2.57	1.00
MgC_6DC	1537.78	1582.06	1574.32	-	44.28	-7.74	-
MgC_7DC	1557.19	1581.18	1575.09	-	23.99	-6.09	-

Note: The change in wavenumber (*Δ*) is calculated as *ν*(final state) - *ν*(initial state). Therefore, a positive value indicates a blueshift (an increase in wavenumber), while a negative value indicates a redshift (a decrease in wavenumber).

Supplementary Table 4. Characteristic temperatures and thermodynamic parameters for MgC_nDCs derived from TGA and DSC measurements.

	T_{des} / °C	T_g / °C	T_c / °C	T_d / °C	ΔH_c / kJ·mol^{-1}	ΔS_c / J·mol^{-1}·K^{-1}
MgC_2DC	128	-	307.8	416	29.5	50.47
MgC_3DC	130	268.9	292.4	408	62.9	111.23
MgC_4DC	125	250.5	283.3	323	12.6	22.58
MgC_5DC	154	248.8	295.5	325	18.8	33.02
MgC_6DC	150	245.7	-	332	-	-
MgC_7DC[a]	153	223.4	-	340	-	-

[a] For MgC_7DC, additional transitions were observed: T_g^{mq} = 205.2 °C, T_{lc} = 285.4 °C, and T_m = 314.3 °C.

Supplementary Table 5. Summary of mechanical properties and corresponding nanoindentation parameters for the MgC_nDC hybrid glasses.

	H / GPa	*E* / GPa	Max. load / mN	Indentation depth / nm	Sinus amplitude / mN [a]
desG-MgC_4DC	0.85	19.50	15	700	1.5
desG-MgC_5DC	0.92	17.48	15	800	1.5
desG-MgC_6DC	2.19	58.09	80	1200	8
mqG-MgC_7DC	0.10	2.60	5	800	5

[a] Sinus frequency = 20 Hz

Supplementary Figures

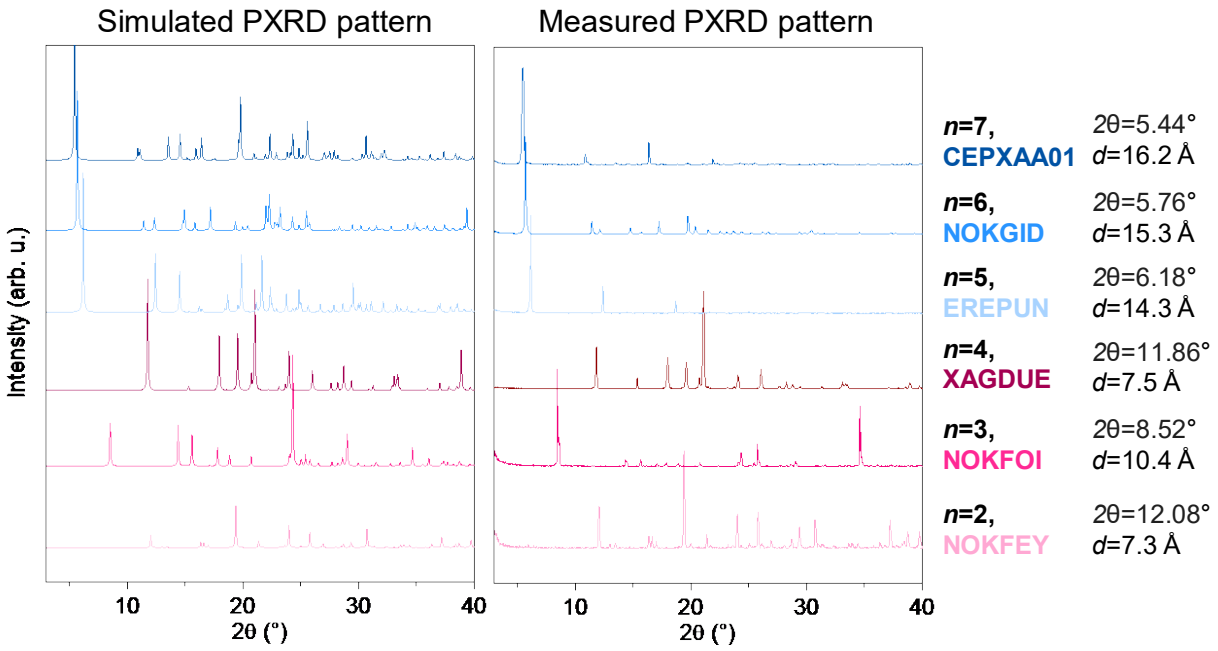

Supplementary Fig. 1 (Left) XRPD patterns simulated from the single-crystal structures of the ***C***-MgC$_n$DC series (n = 2–7). **(Right)** Experimental XRPD patterns of the synthesised ***C***-MgC$_n$DCs. The CCDC reference code and the calculated 2θ position of the lowest-angle diffraction peak with its corresponding d-spacing are indicated. The close agreement between the two sets of patterns confirms the phase purity of the synthesised materials. All data were simulated or measured using Cu K$_\alpha$ (λ = 1.5406 Å).

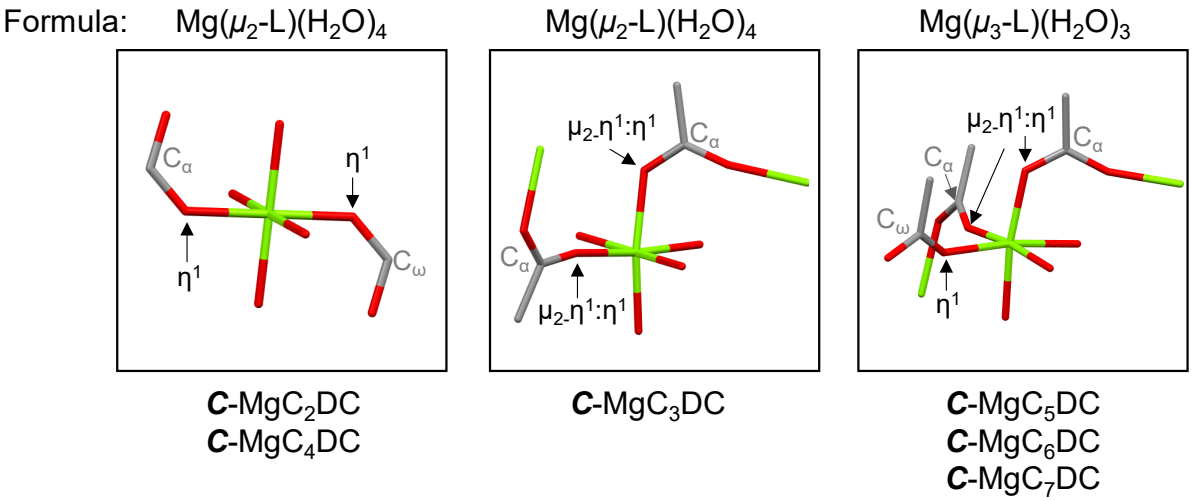

Supplementary Fig. 2 Coordination environments in the ***C***-MgC$_n$DC series. Representative coordination environments of the Mg^{2+} nodes, showing the three distinct types based on methylene chain length, *n*. In these representations, oxygens atoms from the terminal carboxylate groups are indicated by arrows, while the unlabeled oxygen atoms belong to coordinated water. All hydrogen atoms have been omitted for clarity.

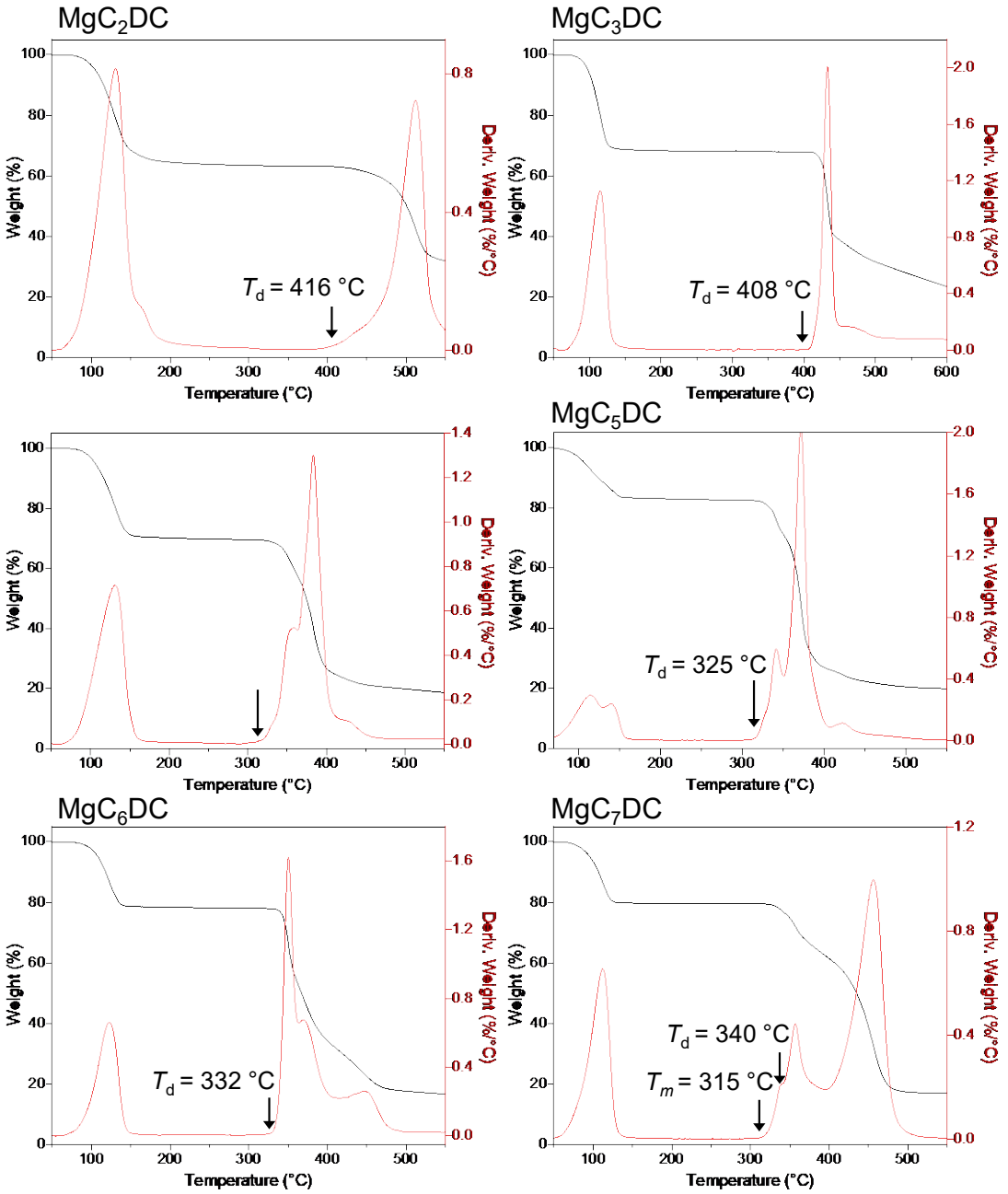

Supplementary Fig. 3 TGA curves (black) and their first derivatives (red) for the ***C***-MgC$_n$DC series. The measurements were conducted under a nitrogen atmosphere at a heating rate of 10 °C·min^{-1}. The decomposition temperature (T_d), determined from the onset point of the major weight loss step, is indicated by an arrow. For MgC$_7$DC, the melting temperature (T_m) observed prior to decomposition is also indicated.

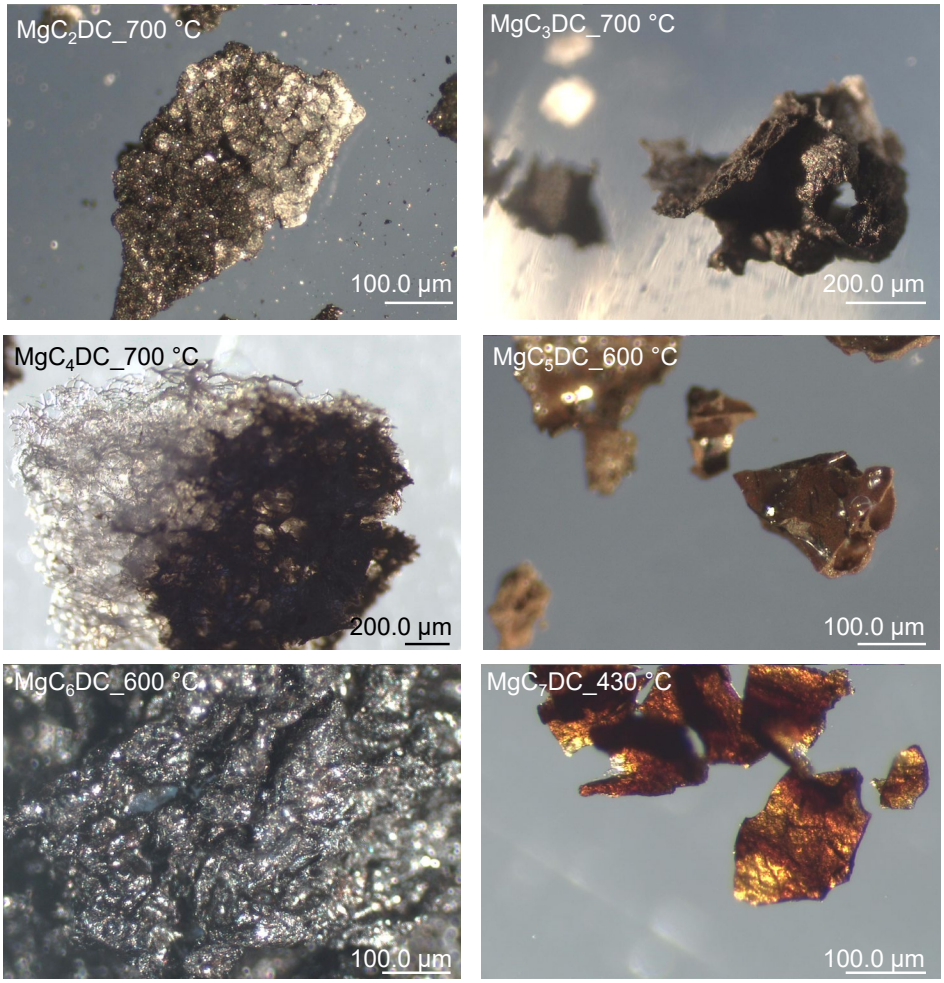

Supplementary Fig. 4 Optical microscopy images showing the puffed and sintered morphology of thermally decomposed MgC_nDCs residues after TGA analysis. The temperature noted in each micrograph indicates the final temperature of the heat treatment.

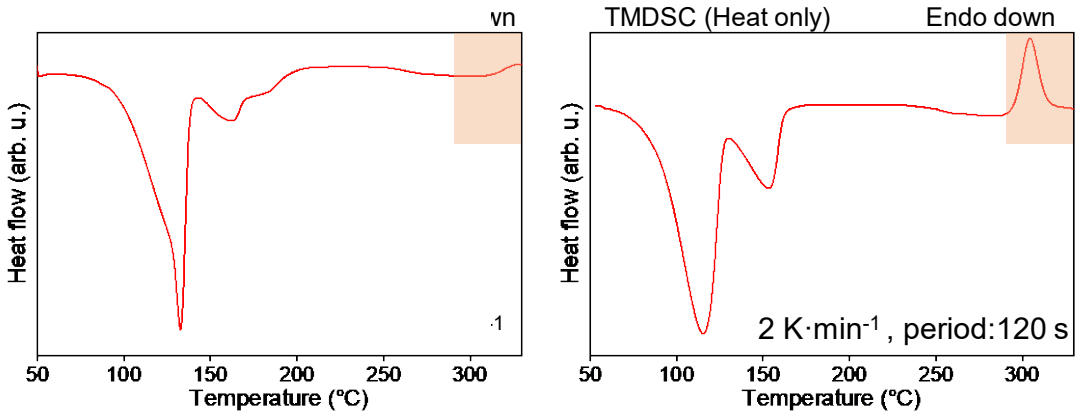

Supplementary Fig. 5 A comparison between **(Left)** a conventional DSC curve (10 K·min^{-1} heating rate) and **(Right)** a $\mathbf{HF}_{tot}$ curve measured by TMDSC (heat-only, 2 K·min^{-1} heating rate) for ***C***-MgC_5DC. The TMDSC data clearly resolves a weak exothermic peak corresponding to the cold crystallisation transition near 300 °C (highlighted), which is not apparent in the conventional DSC measurement.

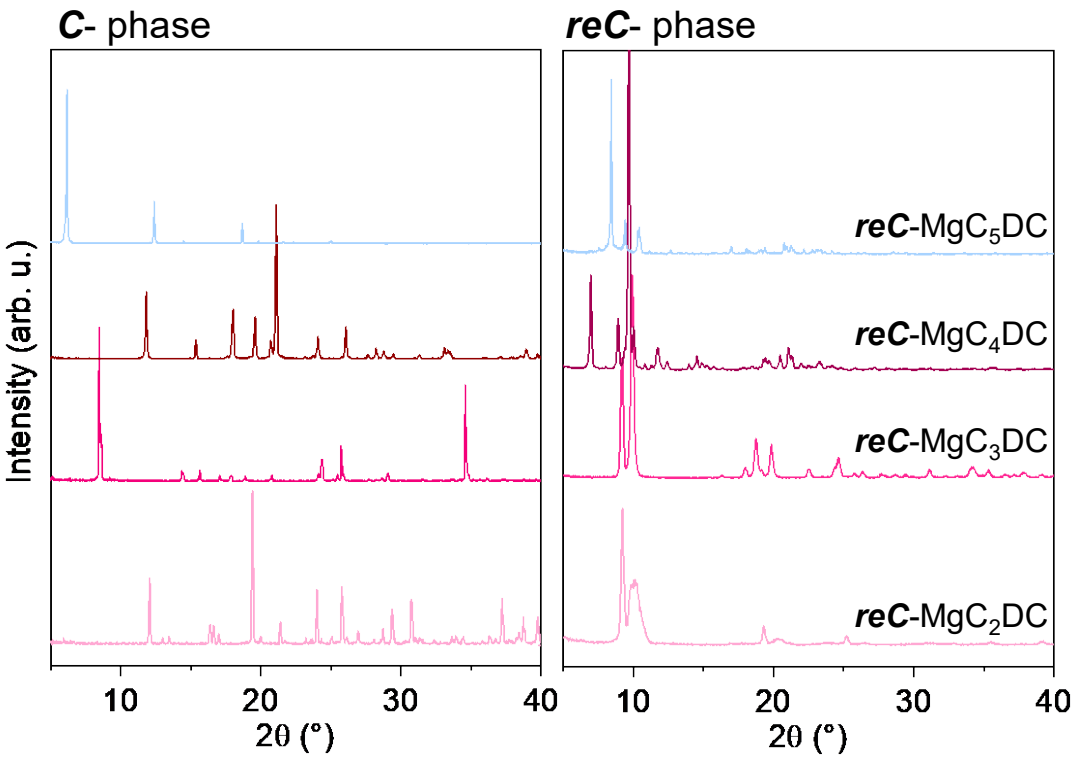

Supplementary Fig. 6 (Left) Experimental XRPD patterns of the synthesised ***C***-MgC$_n$DCs (n = 2–5). **(Right)** Experimental XRPD patterns of the thermal conversed ***reC***-MgC$_n$DCs. All data were simulated or measured using Cu K_α (λ = 1.5406 Å).

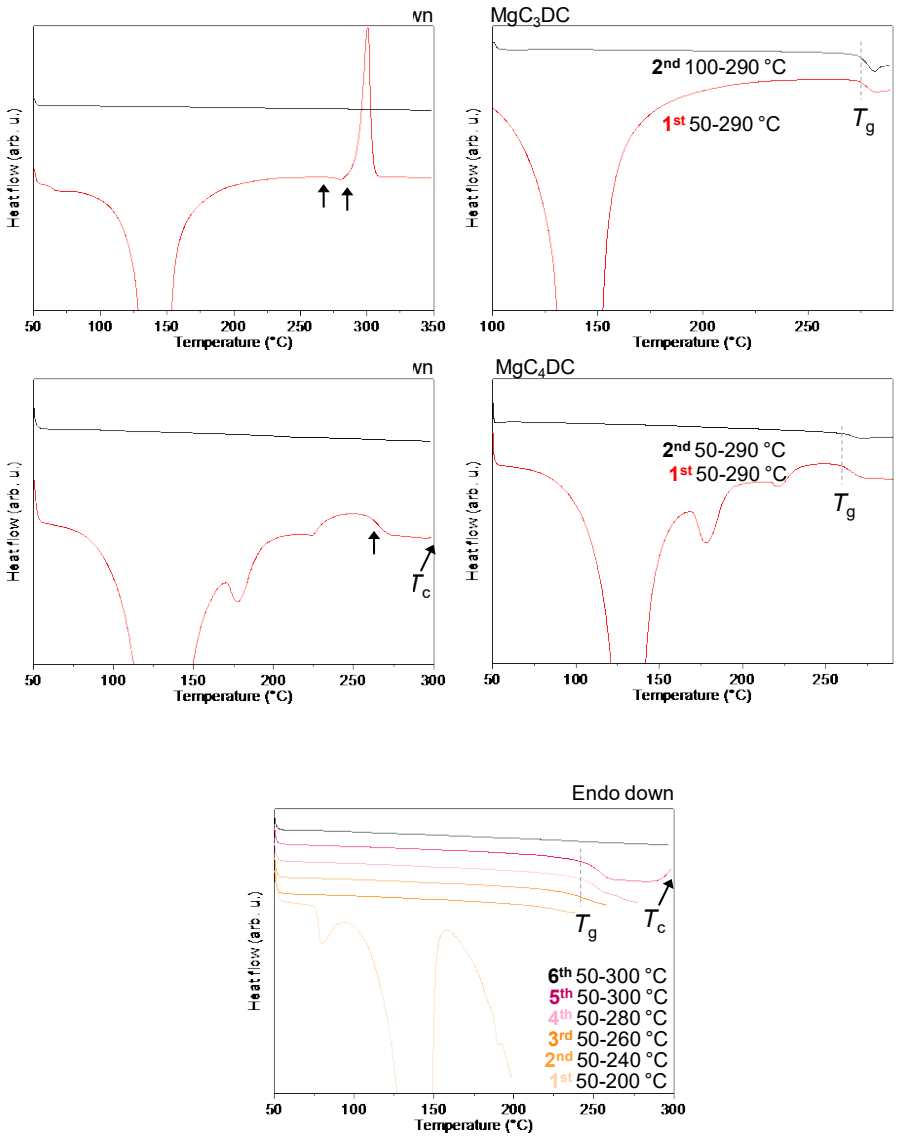

Supplementary Fig. 7 (a) DSC curves for MgC_3DC and MgC_4DC. The right panels show a reversible glass transition at T_g upon reheating, which occurs when the samples are first heated to a temperature below their cold crystallisation temperature (T_c). The left panels show that after heating above T_c, the T_g is absent in subsequent cycles. **(b)** Consecutive DSC heating runs for MgC_5DC with progressively increasing maximum temperatures. The T_g is observed reversibly up to 280 °C (below its T_g) but vanishes permanently after the sample is heated to 300 °C (above its T_c). These results confirm that cold crystallisation is an irreversible process and that the resulting ***reC***- phase does not exhibit a glass transition.

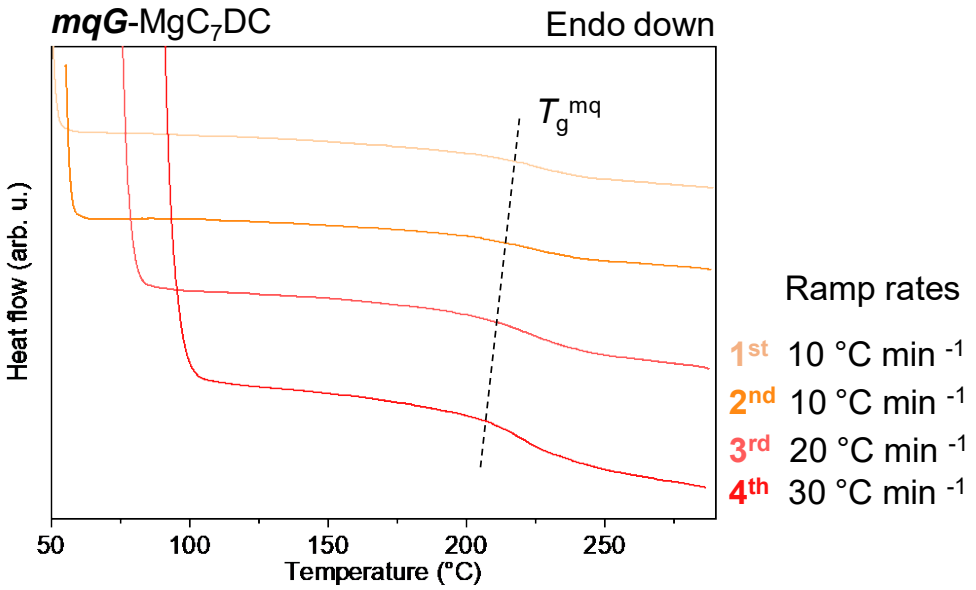

Supplementary Fig. 8 DSC curves for ***mqG***-MgC_7DC with various heat rates. The dotted lines indicate the glass transition temperature (T_g^{mq}). As the heating rate increases, T_g^{mq} shifts to a higher temperature and the magnitude of the baseline shift increases. This kinetic dependence is a characteristic signature of a glass transition.

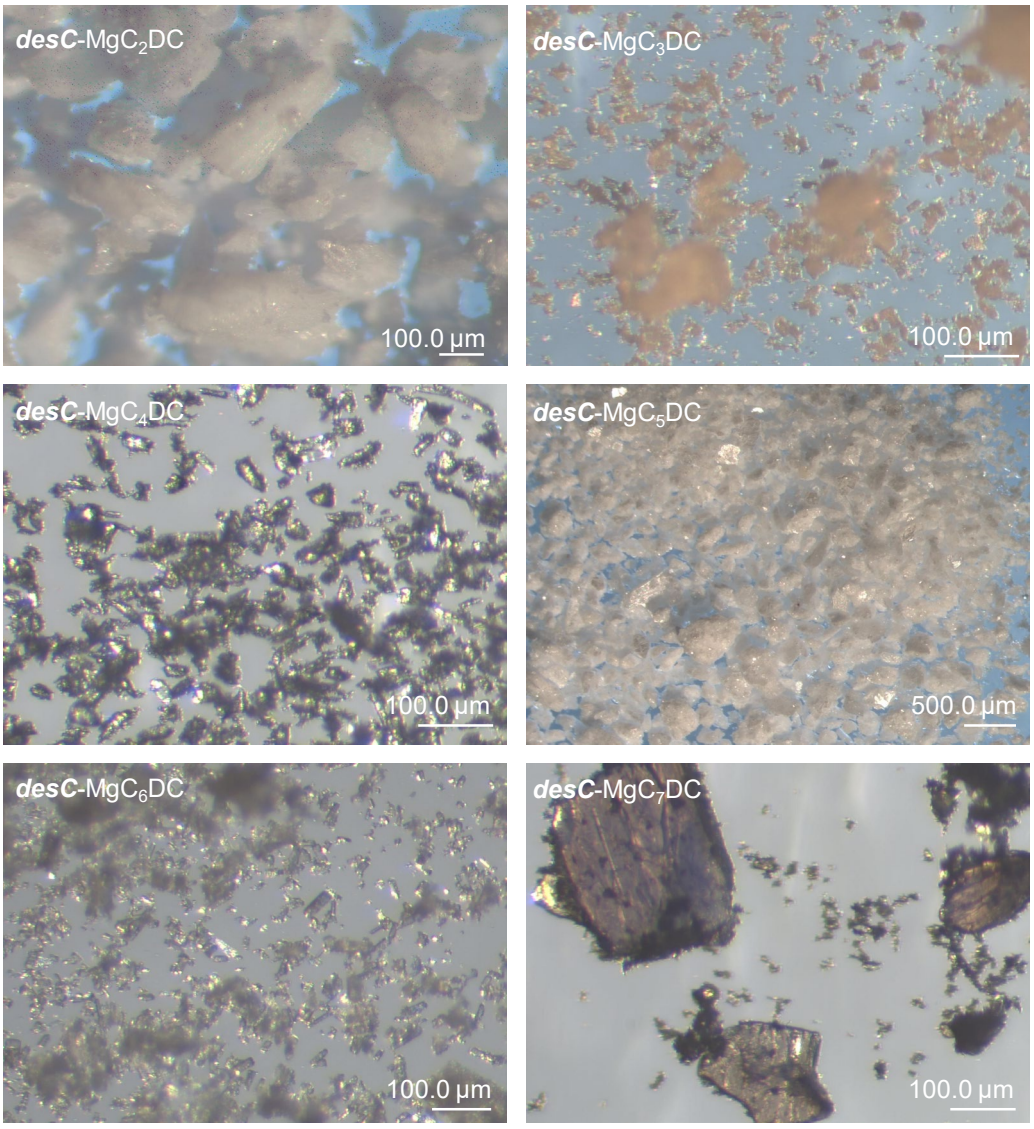

Supplementary Fig. 9 Optical microscopy Images of the ***desC***-MgC_nDCs, confirming that all ***desC***- phases retain a crystalline and powdery nature after the desolvation process.

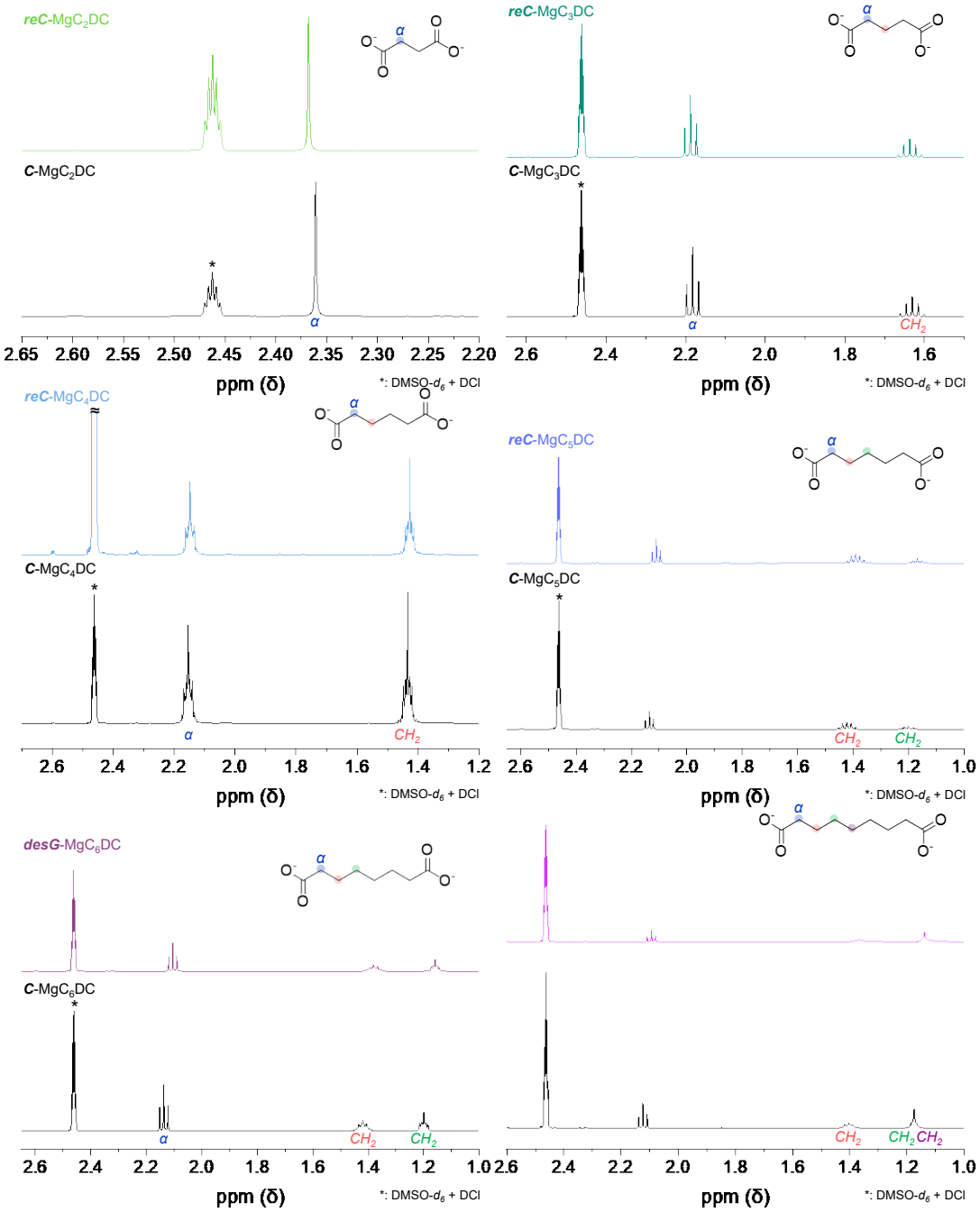

Supplementary Fig. 10 ^{1}H NMR spectra for the initial ***C***-MgC$_n$DCs and their corresponding thermally treated phases (***reC***-, ***desG***-, or ***mqG***-). The peaks of the dicarboxylate ligands are present in all spectra, confirming that the ligands remain intact within glassy phases.

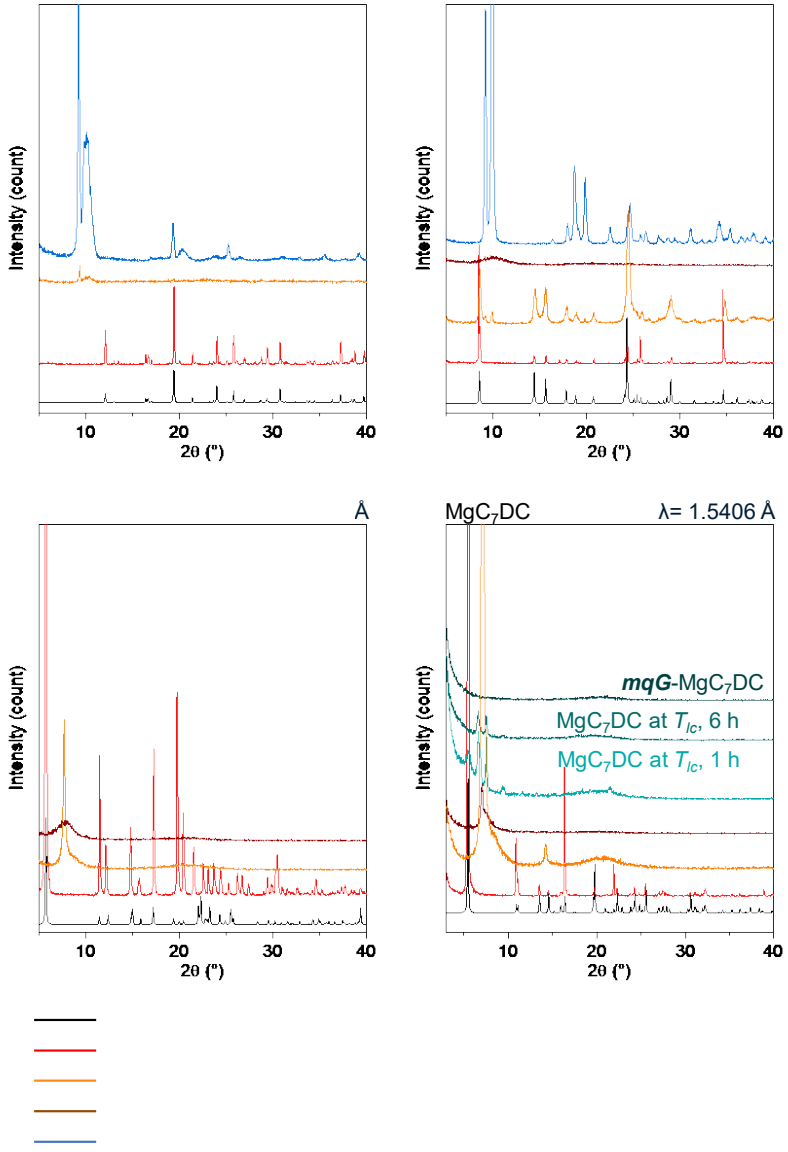

Supplementary Fig. 11 Ex-situ XRPD patterns are shown for various phases of MgC_2DC, MgC_3DC, MgC_6DC, and MgC_7DC. The bottom-right panel focuses on MgC_7DC, showing the patterns of the quenched ***LC***- phase after being held at T_{lc} for 1 and 6 hours, as well as the pattern of the ***mqG***- phase.

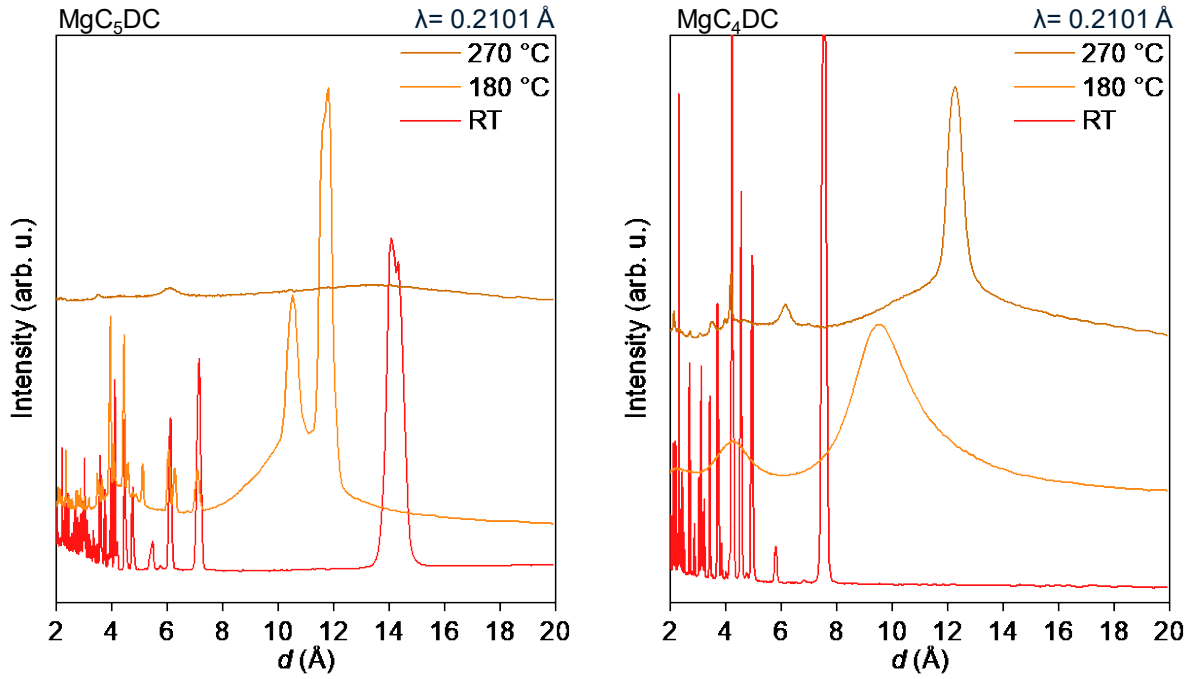

Supplementary Fig. 12 Variable-temperature in-situ XRPD patterns showing the structural evolution of **(Left)** MgC_5DC and **(Right)** MgC_4DC. The patterns were collected sequentially after a 15-minute isothermal hold at key temperatures corresponding to the ***C***- phase (room temperature), the ***desC***- phase (180 °C), and the ***desL***- phase (270 °C).

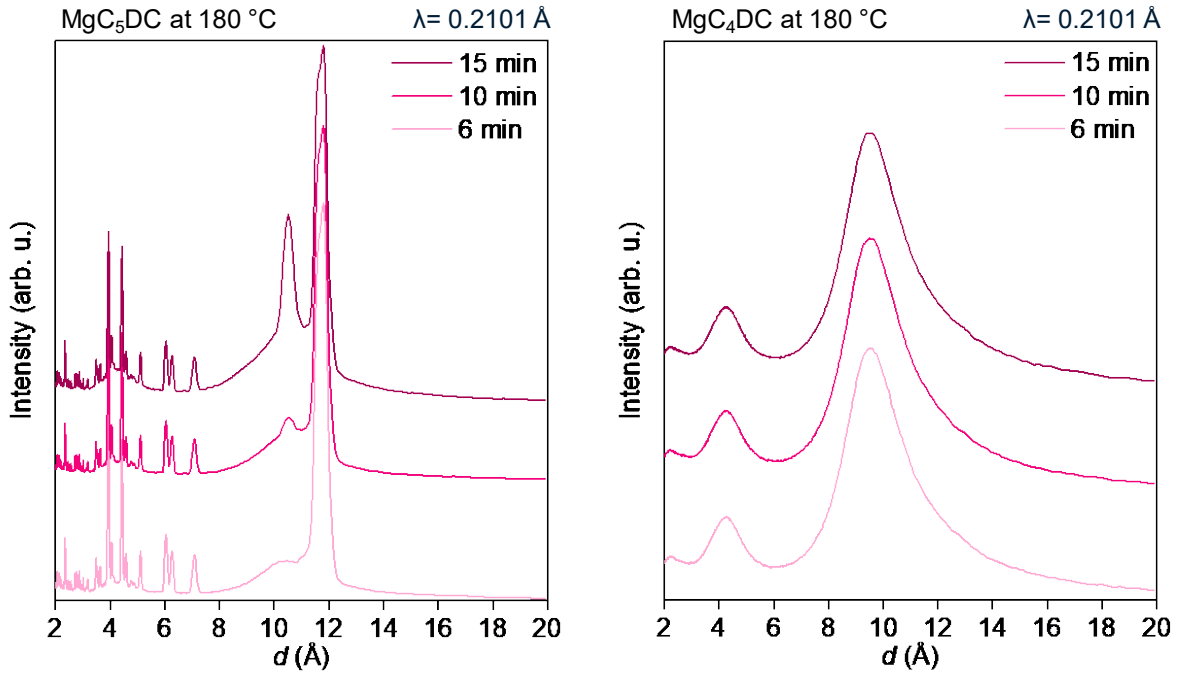

Supplementary Fig. 13 Time-resolved in-situ XRPD patterns of MgC_5DC and MgC_4DC during the isothermal hold at 180 °C, illustrating their different desolvation kinetics. The patterns for the lamellar ***desC***-MgC_5DC evolve gradually over time, showing the slow removal of the condensed hydrophilic layer. In contrast, the patterns for ***desC***-MgC_4DC remain static, as its transformation to the ***desC***- phase was already complete upon reaching 180 °C.

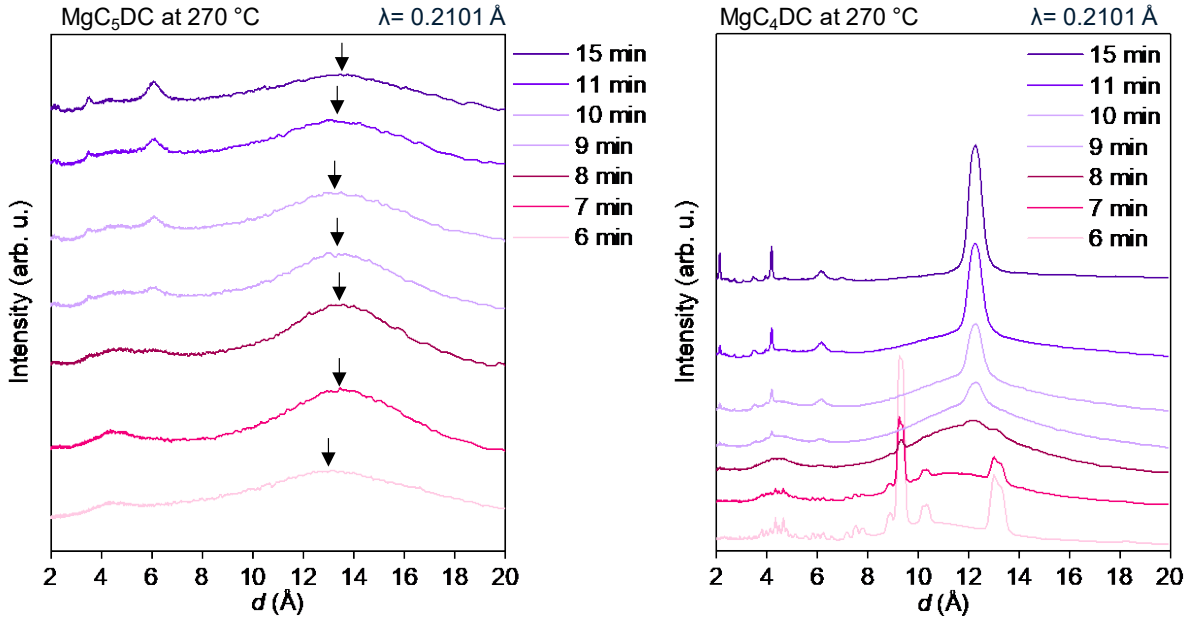

Supplementary Fig. 14 Time-resolved in-situ XRPD patterns of MgC_5DC and MgC_4DC during the isothermal hold at 270 °C, illustrating the dynamic nature of their ***desL***- phase. The broad FSDP peaks and their fluctuations over time in both samples are characteristic of the high chain mobility in the supercooled liquid state. The arrows for MgC_5DC highlight the fluctuation of the peak corresponding to medium-range order, providing direct evidence of the fluidic lamellar structure.

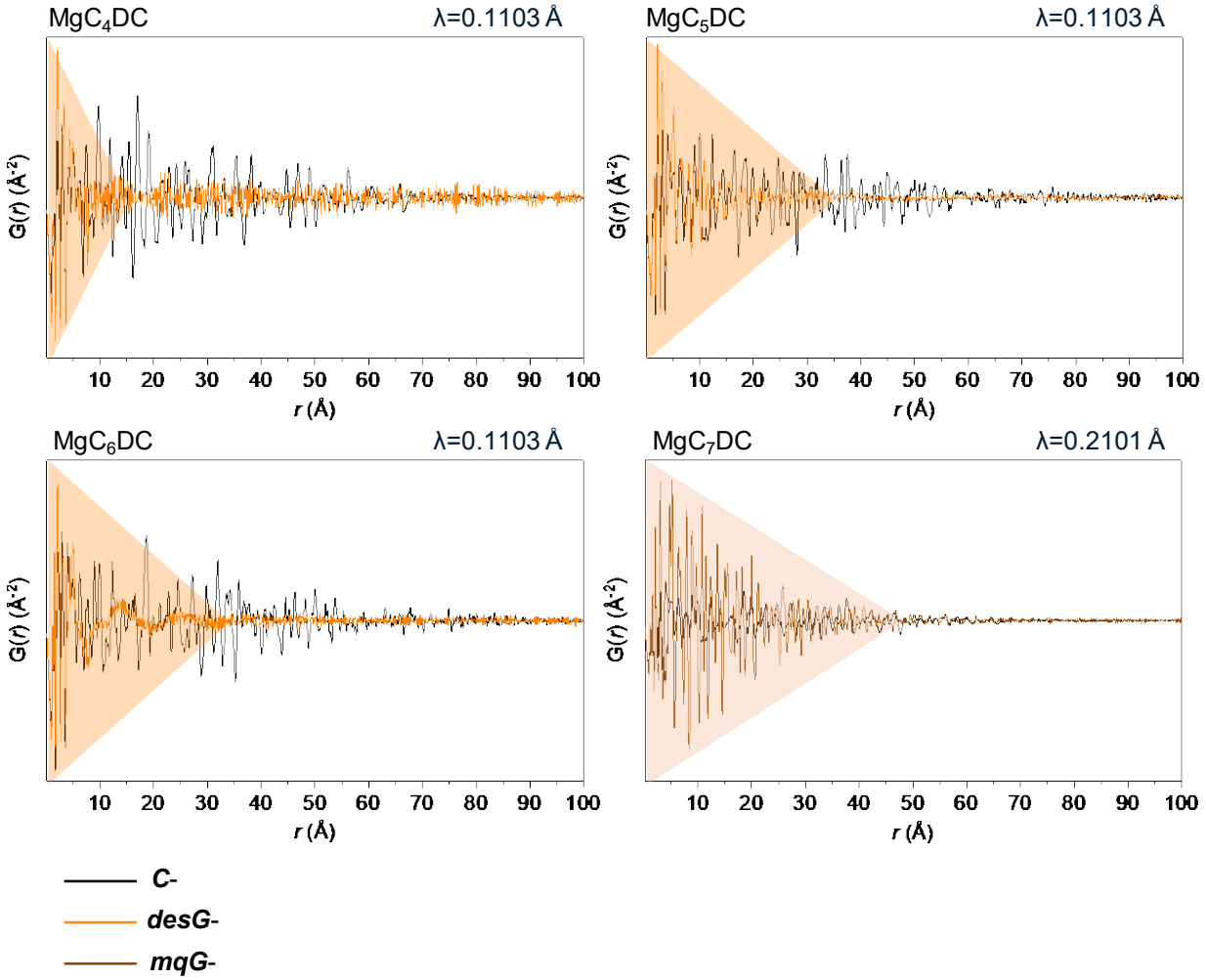

Supplementary Fig. 15 Experimental PDF data, G(*r*), covering the range of 0.1–100 Å are presented for the ***C***-MgC$_n$DC (*n* = 4–7), ***desG***-MgC$_n$DC (*n* = 4–6), and ***mqG***-MgC$_7$DC phases. The shaded area highlights the persistence of medium- and long-range order in the glassy MgC$_n$DCs, confirming that the glasses retain an extended coordination network even though their XRPD patterns appear amorphous.

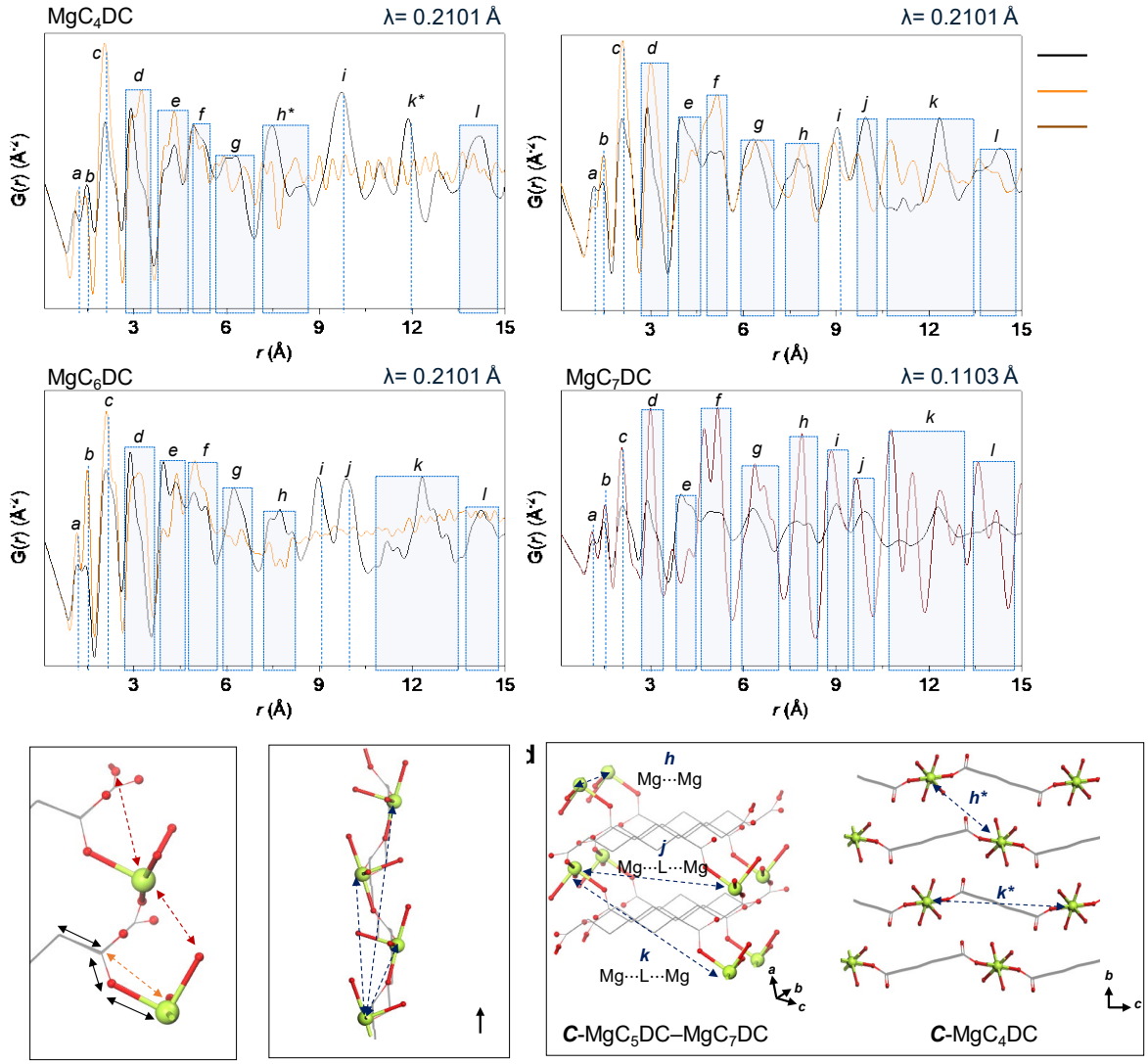

Supplementary Fig. 16 Analysis of the local structure of MgC_nDCs by assigning PDF correlations. **(a)** Measured PDF data for the initial crystal (***C***-) and glassy (***desG-*** and ***mqG***-) MgC_nDC (n = 4–7), covering the short- and medium-range order region (r = 0.1–15 Å). The alphabet-labelled peaks correspond to the specific atomic correlations illustrated below. **(b-d)** Illustrations of structural features based on the single crystal structures: **(b)** the short-range order (up to ~5 Å) representing the Mg coordination environment; **(c)** the Mg···Mg correlations within the 1D chain network; **(d)** medium-range Mg···Mg correlations, distinguishing between interchain distances (h, h*) and those bridged by a single linker (j, k, k*). The preservation of these correlations in the corresponding glassy phases confirms that this local and medium-range order is largely retained during vitrification.

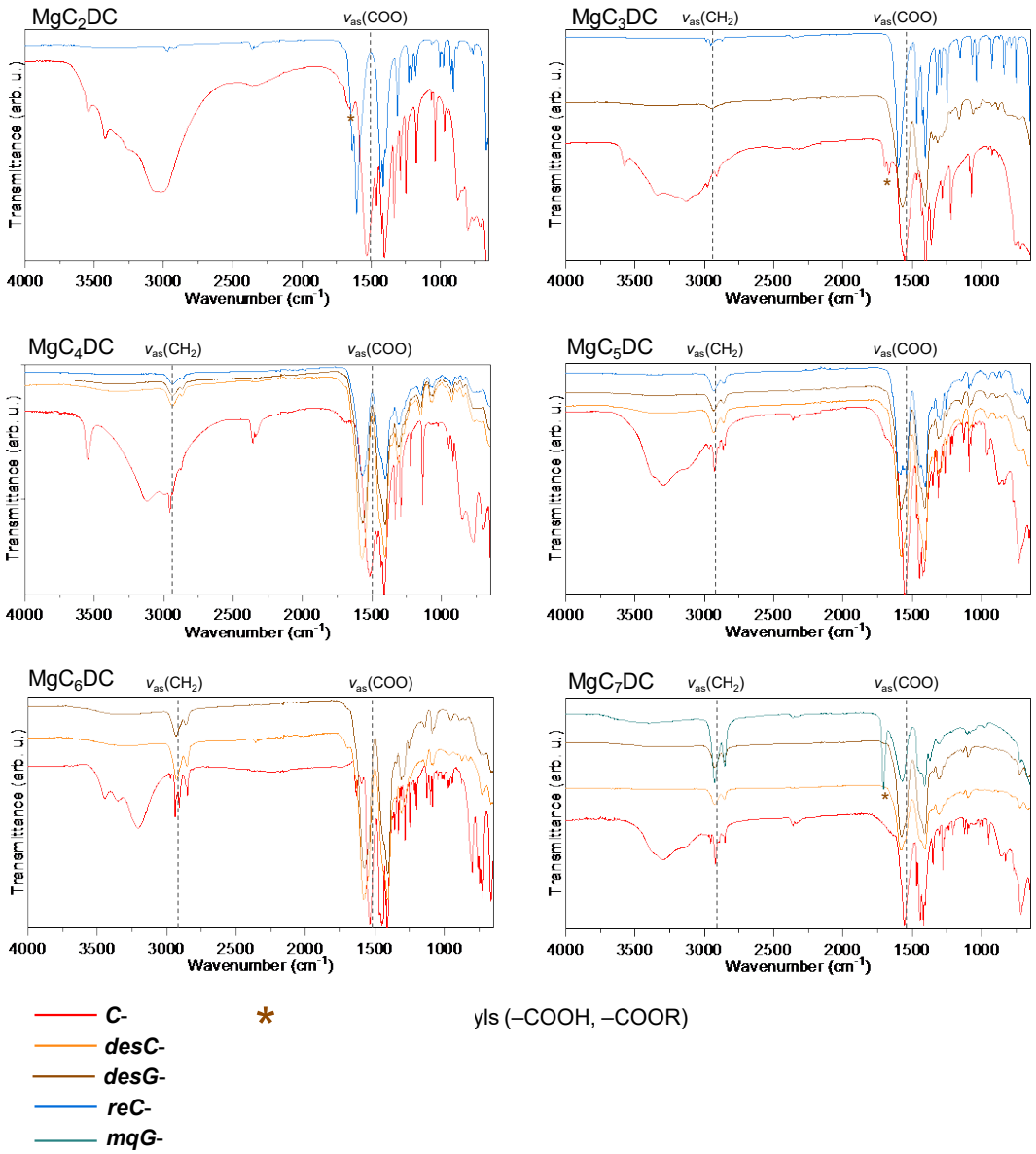

Supplementary Fig. 17 FTIR spectra of MgC_nDCs across different phases. The spectra for the ***C***-, ***desC***-, ***desG***-, ***reC***-, and ***mqG***- phases. The grey dotted lines indicate the peak positions of the asymmetric stretching modes of the methylene and carbonyl groups. The asterisk (*) indicates the peak corresponding to non-ionised carbonyl groups, observed in ***C***-MgC_2DC, ***C***-MgC_3DC, and ***mqG***-MgC_7DC.

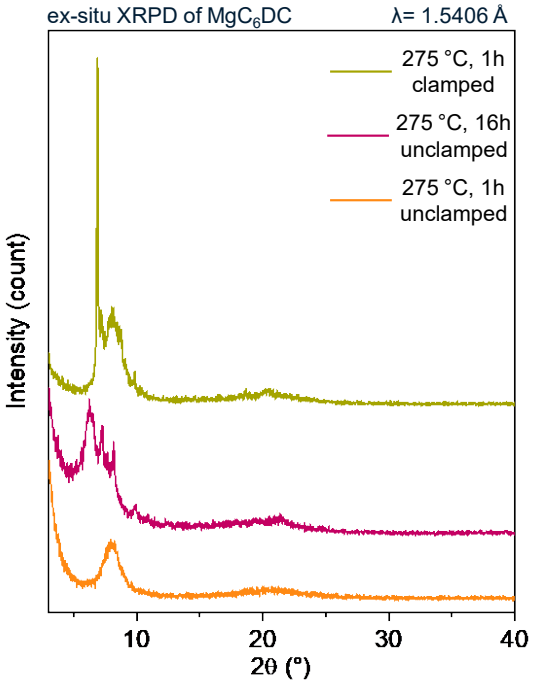

Supplementary Fig. 18 Ex-situ XRPD data for MgC_6DC samples thermally treated at 275 °C under different conditions. A clamped sample was prepared by clamping ***C***-MgC_6DC powder between glass slides using forceps and subsequently subjecting it to the thermal process. While the sample remains amorphous after 1 hour of heating without pressure, both prolonged heating (16 h) and applied pressure (1 h) induce the formation of a crystalline phase.

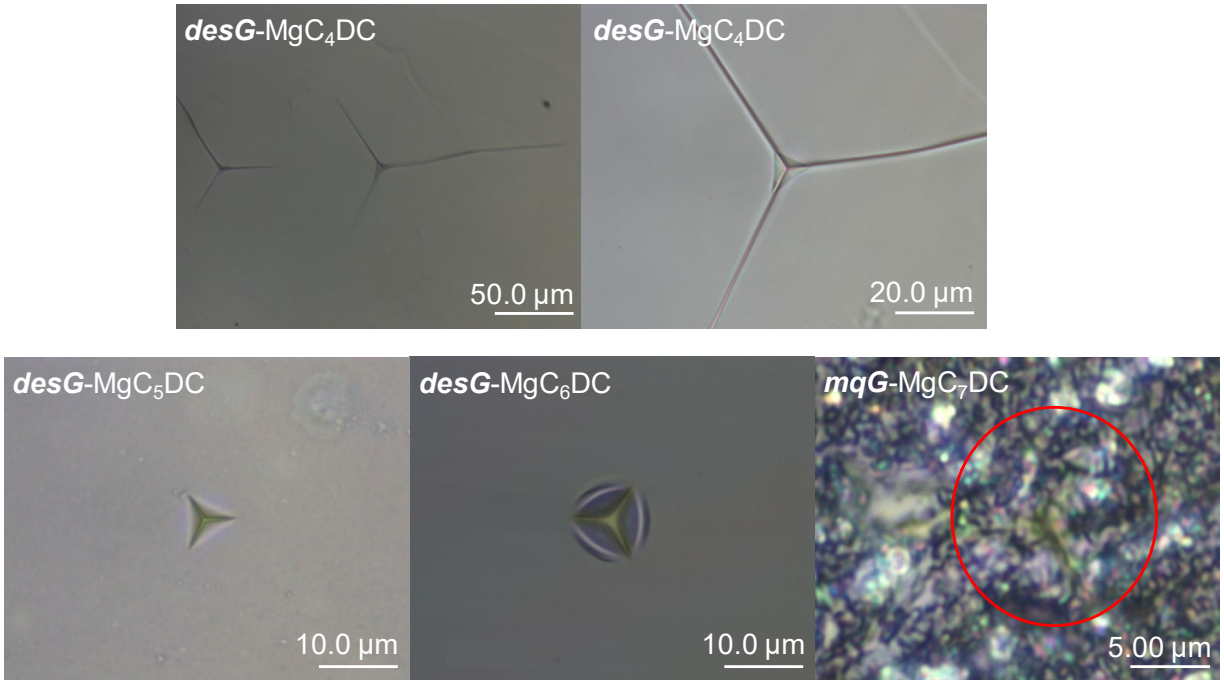

Supplementary Fig. 19 Optical microscopy images of glassy MgC_nDC samples (n = 4–7) showing residual impressions after nanoindentation. Crack propagation from the indent corners was observed only in ***desG***-MgC_4DC, suggesting the presence of brittle crystallites in this sample, despite its amorphous nature as confirmed by XRPD. In contrast, other samples, such as ***desG***-MgC_6DC, exhibit sink-in behaviour without cracking, indicating a monolithic character. The red circle highlights the contacted zone for the ***mqG***-MgC_7DC sample.

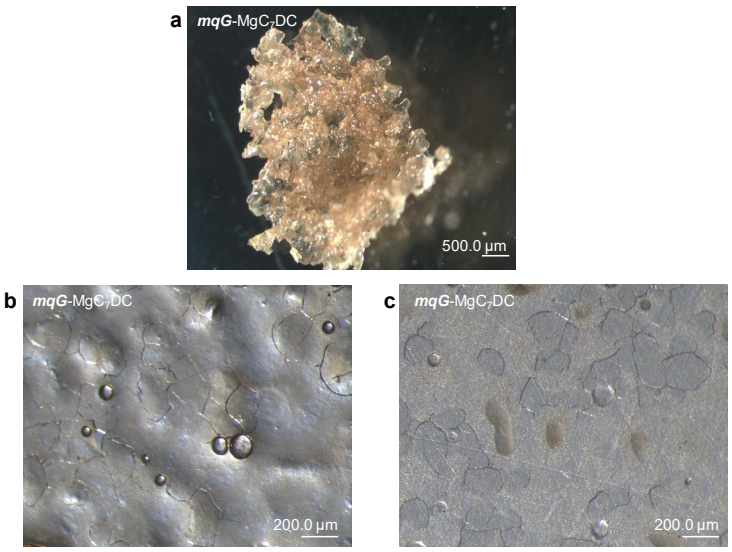

Supplementary Fig. 20 Optical microscopy images of ***mqG***-MgC_7DC. **(a)** A bulk sample of ***mqG***-MgC_7DC after treatment at 320 °C for 20 min. The observed colour change to brown and the increase in bubble size suggest partial ligand decomposition. **(b)** The appearance of an as-processed ***mqG***-MgC_7DC sample prepared on a glass slide for mechanical property measurements. **(c)** The surface of the same sample after being polished and washed with acetone.

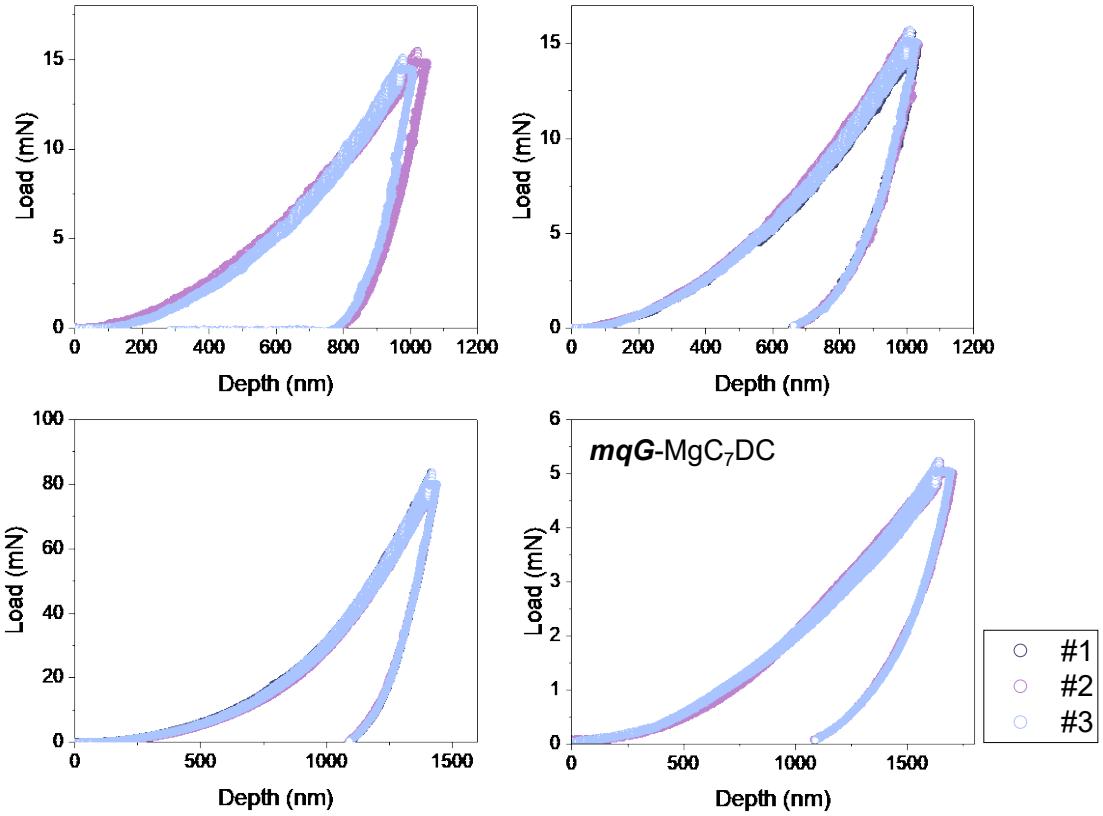

Supplementary Fig. 21 Load-depth curves for the indicated hybrid glass samples, obtained from nanoindentation measurements. The different coloured circles in each plot represent independent measurements (#1, #2, #3) performed at different locations on the same sample, demonstrating the reproducibility of the data. Three measurements were taken for each sample, except for ***desG***-MgC$_4$DC (two measurements).

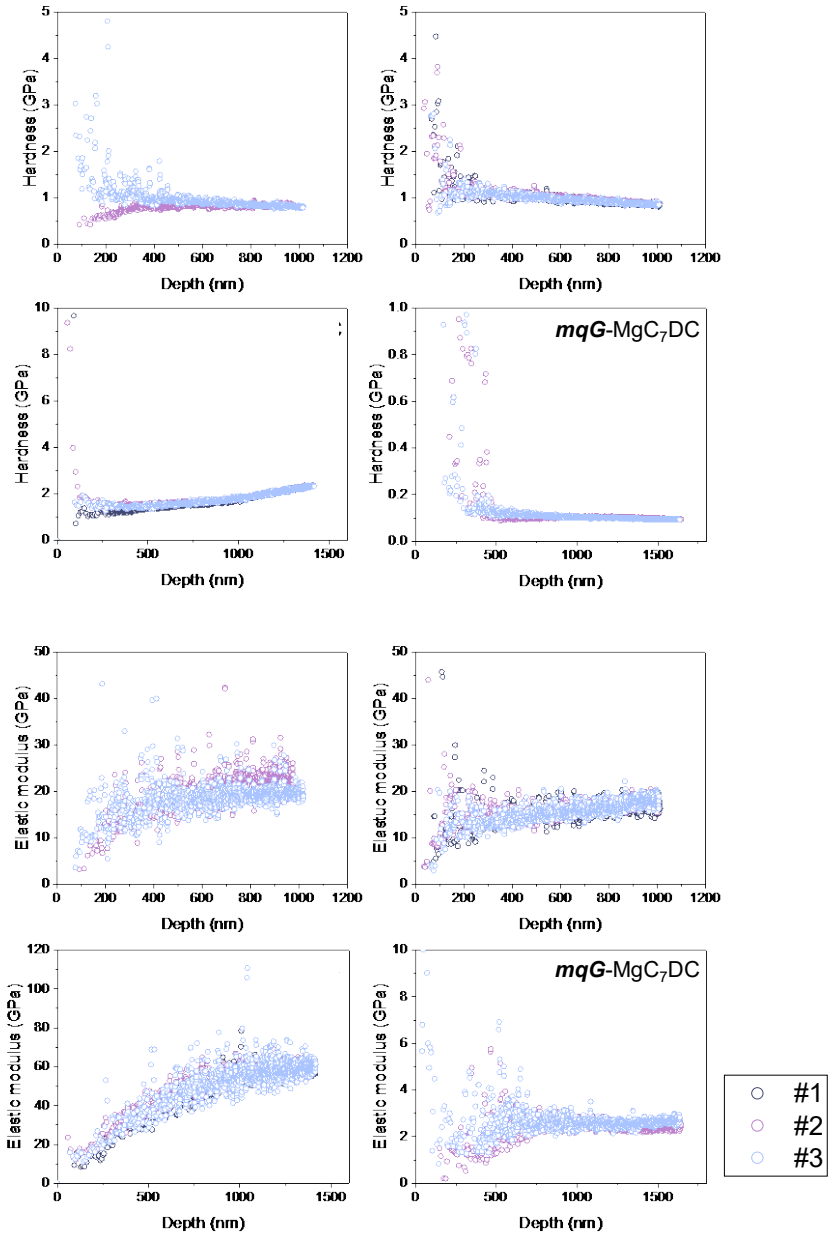

Supplementary Fig. 22 Plots of hardness (**a**) and elastic modulus (**b**) as a function of indentation depth for the indicated glass samples. These values were calculated from the load-depth curves shown in Supplementary Fig. 21. The representative values are summarized in Supplementary Table 3, and they were determined from the plateau region of these curves.

Supplementary References [1–17]

1. Jiang, Z., Imrie, C. T. & Hutchinson, J. M. An introduction to temperature modulated differential scanning calorimetry (TMDSC): a relatively non-mathematical approach. *Thermochimica Acta* **387**, 75–93 (2002).
2. Fleck, M., Tillmanns, E. & Haussühl, S. Crystal structure of tetraaquamagnesium adipate, Mg(H2O)4(C6H8O4). *Zeitschrift für Kristallographie - New Crystal Structures* **215**, 107–108 (2000).
3. Frey, M. *et al.* Determining the fragility of bulk metallic glass forming liquids via modulated DSC. *J. Phys.: Condens. Matter* **32**, 324004 (2020).
4. Kawaguchi, S. *et al.* High-throughput and high-resolution powder X-ray diffractometer consisting of six sets of 2D CdTe detectors with variable sample-to-detector distance and innovative automation system. *J Synchrotron Rad* **31**, 955–967 (2024).
5. Corkery, R. W. Metal organic framework (MOF) liquid crystals. 1D, 2D and 3D ionic coordination polymer structures in the thermotropic mesophases of metal soaps, including alkaline earth, transition metal and lanthanide soaps. *Current Opinion in Colloid & Interface Science* **13**, 288–302 (2008).
6. Quaresma, S. *et al.* Novel Antibacterial Azelaic Acid BioMOFs. *Crystal Growth & Design* **20**, 370–382 (2020).
7. Stepniewska, M. *et al.* Observation of indentation-induced shear bands in a metal−organic framework glass. *Proceedings of the National Academy of Sciences* **117**, 10149–10154 (2020).
8. Guo, X.-X. & Lin, J. Poly[hexa-aqua-bis-(μ3-hepta-nedioato-κ3O:O′:O″)dimagnesium]. *Acta Cryst E* **67**, m665–m665 (2011).
9. Schawe, J. E. K. Principles for the interpretation of temperature-modulated DSC measurements. Part 2: A thermodynamic approach. *Thermochimica Acta* **304–305**, 111–119 (1997).
10. Gallington, L. C., Wilke, S. K., Kohara, S. & Benmore, C. J. Review of Current Software for Analyzing Total X-ray Scattering Data from Liquids. *Quantum Beam Science* **7**, 20 (2023).
11. Terban, M. W. & Billinge, S. J. L. Structural Analysis of Molecular Materials Using the Pair Distribution Function. *Chem. Rev.* **122**, 1208–1272 (2022).

12. Sauer, B. B., Kampert, W. G., Neal Blanchard, E., Threefoot, S. A. & Hsiao, B. S. Temperature modulated DSC studies of melting and recrystallization in polymers exhibiting multiple endotherms. *Polymer* **41**, 1099–1108 (2000).
13. Pyda, M. Temperature-Modulated Differential Scanning Calorimetry. in *Encyclopedia of Polymer Science and Technology* 1–31 (John Wiley & Sons, Ltd, 2014). doi:10.1002/0471440264.pst623.
14. Nelson, P. N. & Taylor, R. A. Theories and experimental investigations of the structural and thermotropic mesomorphic phase behaviors of metal carboxylates. *Appl Petrochem Res* **4**, 253–285 (2014).
15. Ohara, K. *et al.* Time-resolved pair distribution function analysis of disordered materials on beamlines BL04B2 and BL08W at SPring-8. *J Synchrotron Rad* **25**, 1627–1633 (2018).
16. Zheng, Q. *et al.* Understanding Glass through Differential Scanning Calorimetry. *Chem. Rev.* **119**, 7848–7939 (2019).
17. Mauro, J. C., Yue, Y., Ellison, A. J., Gupta, P. K. & Allan, D. C. Viscosity of glass-forming liquids. *Proceedings of the National Academy of Sciences* **106**, 19780–19784 (2009).